nature physics

SUPPLEMENTARY INFORMATION

DOI: 10.1038/NPHYS3565

Cassini *in situ* observations of long-duration magnetic re-connection in Saturn's magnetotail

C.S. Arridge[1], J.P. Eastwood[2], C.M. Jackman[3], G.-K. Poh[4], J.A. Slavin[4], M.F. Thomsen[5], N. André[6], X. Jia[4], A. Kidder[7], L. Lamy[8], A. Radioti[9], N. Sergis[10], M. Volwerk[11], A.P. Walsh[12], P. Zarka[8], A.J. Coates[13], M.K. Dougherty[2]

1. Department of Physics, Lancaster University, Bailrigg, Lancaster, LA1 4YB, United Kingdom.

2. Department of Physics, Imperial College, South Kensington, London, SW7 2BW, United Kingdom.

3. School of Physics and Astronomy, University of Southampton, Southampton, SO17 1BJ, United Kingdom.

4. Department of Atmospheric, Oceanic and Space Sciences, University of Michigan, 2455 Hayward St., Ann Arbor, Michigan 48109-2143, USA

5. Planetary Science Institute, 1700 East Fort Lowell, Suite 106, Tucson, Arizona 85719-2395, USA.

6. CNRS, Institut de Recherche en Astrophysiqe et Planétologie, 9 avenue du colonel Roche, BP 44346, 31028 Toulouse Cedex 4, France.

7. Department of Earth and Space Sciences, University of Washington, Box 351310, Seattle, Washington 98195, USA.

8. LESIA-Observatoire de Paris, CNRS, UPMC Univ. Paris 6, Univ. Paris-Diderot, 92195, Meudon, France.

9. Laboratoire de Physique, Atmosphérique et Planétaire, Institut d'Astrophysique et de Géophysique, Université de Liège, Liège, Belgium.

10. Office for Space Research, Academy of Athens, 4, Soranou Efesiou str., 11527, Papagos, Athens, Greece.

© 2015 Macmillan Publishers Limited. All rights reserved

 DOI: 10.1038/NPHYS3565

11. Austrian Academy of Sciences, Space Research Institute, Schmiedlstraße 6, 8 042 Graz, Austria.

12. Science and Robotic Exploration Directorate, European Space Agency, ESAC, Villanueva de la Cañada, 28692 Madrid, Spain.

13. Mullard Space Science Laboratory, Department of Space and Climate Physics, University College London, Holmbury St. Mary, Dorking, Surrey, RH5 6NT, United Kingdom.

© 2015 Macmillan Publishers Limited. All rights reserved

Trajectory

Figure S1 shows the trajectory of Cassini in Kronocentric Solar Magnetospheric (KSM) coordinates, where the X axis points from Saturn to the Sun, the X-Z plane contains the spin axis of Saturn, and Y points towards dusk. After periapsis with Saturn on 25 September 2006, Cassini started its orbit (Revolution) 30 and moved out into the magnetotail via dusk reaching an apoapsis of 36.6 R_S on 03 October 2006 at 1904 UT at a local time of 00h18m and latitude of 20.9º with the spacecraft moving towards the equator. At the start of the reconnection event at 0146 UT on 08 October 2006 (day of year 281) the spacecraft was at 29.0 R_S, a latitude of 9.25º and local time 01h27m. The KSM coordinates at the start of the reconnection event was (-26.8, -10.6, -2.63) R_S. From figure S1 we can see that the spacecraft was located slightly north of the warped magnetospheric current sheet as can also be seen in the observations (figure 1).

Instrumentation

Data in this study comes from the magnetometer, plasma spectrometer (CAPS), Radio and Plasma Wave Science (RPWS), and Magnetospheric Imaging Instrument (MIMI) instruments on the Cassini spacecraft. Upstream solar wind conditions are obtained from the ENLIL model[1] and are discussed in more detail in the next section.

Magnetometer data are taken from the fluxgate magnetometer instrument at a cadence of 1s in a spherical polar coordinate system centred on the spacecraft (Kronographic Radial-Theta-Phi, KRTP) which is based on the kronographic position of the spacecraft, where the radial vector, $\mathbf{e}_r$, is oriented from the planet to the spacecraft, the polar vector, $\mathbf{e}_\theta$, points in the direction of increasing co-latitude, and the azimuthal vector $\mathbf{e}_\varphi$ completes the right-handed set and is oriented in a prograde direction around Saturn.

© 2015 Macmillan Publishers Limited. All rights reserved

 DOI: 10.1038/NPHYS3565

Plasma data are taken from the CAPS electron spectrometer (ELS) and ion mass spectrometer (IMS) which are electrostatic analysers but where IMS also has a time-of-flight (TOF) section to determine the energy-resolved mass per charge ratio of the incoming ions with a mass/charge resolution of 12.5%. ELS detects electrons between 0.6 and 28750 eV/e in 63 energy bins with a resolution of ΔE/E of 16.7%. The instantaneous field-of-view (FOV) is split into eight 20º×5.2º anodes providing a total 160º×5.2º instantaneous FOV. ELS sweeps this FOV every 2 s but these samples can be averaged on board to lower time and energy resolution. IMS detects positive ions between 1 and 50280 eV/q in 63 energy bins with a resolution of ΔE/E of 16.7% and a cadence of 4 s. Similar to ELS, the instantaneous FOV is split into eight anodes each with an FOV of 20º×8.3º providing a total instantaneous FOV of 160º×5.3º. The FOV of ELS and IMS are approximately boresighted. To improve the FOV the whole CAPS instrument is mounted on a rotating platform which sweeps the sky by around 1º/s, extending the FOV to ~2π sr with a period of ~3 minutes. The spacecraft was also rolling for part of the interval reported in this paper which improves the total field-of-view to almost 4π sr but complicates the analysis as described in the appropriate sections below.

Radio data is provided by the RPWS instrument which includes three nearly orthogonal electric field antennae to detect AC electric fields between 1 Hz and 16 MHz and are particularly processed in this paper to analyse kilometric radio emissions[2].

Solar wind simulations and Cassini remote sensing observations

Since there is no upstream monitor at Saturn models must be used to understand the upstream solar wind and interplanetary magnetic field (IMF) conditions while the spacecraft is inside the magnetosphere, as it was during this event. The MSWiM model is

© 2015 Macmillan Publishers Limited. All rights reserved

a 1.5-d MHD propagation of solar wind conditions measured at 1 AU but is only usable near apparent opposition which occurred on 25 February 2006. During the October 2006 time period Saturn is far from apparent opposition and so this model is not reliable. ENLIL is a 3D MHD simulation of the heliosphere[1] which is available at the Community Coordinated Modeling Center (CCMC) at NASA Goddard Space Flight Center. This model is not hampered by the same opposition viewing effects as MSWiM. The model inner boundary condition is provided by coronal models, driven by observed magnetograms, and is placed at 21.5 or 30 solar radii depending on the coronal model. Although limited validation studies of ENLIL have been performed for the outer heliosphere near Saturn, uncertainties on the arrival times for stream interaction regions can be up to four days at 5 AU, from a comparison of ENLIL results with Ulysses data[3]. In this work, version 2.7 of ENLIL was run with an inner boundary condition provided by the Wang-Sheely-Arge model for Carrington rotation 2048 and provided solar wind simulation results at Saturn's position from 21 September to 24 October 2006. In order to properly compare the in situ Cassini data with the ENLIL results we use Cassini observations of auroral radio emissions (Saturn Kilometric Radiation, SKR), known to brighten in response to solar wind compression[4,5]. These observations are used to identify a time shift that can be applied to the ENLIL results.

Figure S2 contains a summary of Cassini radio and plasma wave observations and ENLIL solar wind simulations for the period covering the event. The unshifted ENLIL data is shown in blue and the shifted data (discussed below) is in black. The interval encompasses a corotating interaction region (CIR) where the pressure and magnetic field strength increase. Four crossings of the heliospheric current sheet (HCS) are identified from reversals in the B_T component of the magnetic field in Radial-Tangential-Normal (RTN) coordinates. Such crossings are typically embedded within CIR compressions at

© 2015 Macmillan Publishers Limited. All rights reserved

 DOI: 10.1038/NPHYS3565

Saturn. The presence of a forward shock (FS) from an increase in the solar wind speed and a coincident increase in the dynamic pressure is also identified.

Turning to the Cassini Radio and Plasma Wave (RPWS) data in figures S2a and S2b: prior to the event on 08 October the flux density displays periodic increases in flux as commonly found in Saturn's magnetosphere[2] and has a right-hand circular polarisation consistent with extraordinary mode emission from the northern hemisphere, as expected from Cassini's northern latitude (figure S2c). These periodic emissions are found to occur at the expected phase for northern SKR emissions, labelled N at the top of figure S2a (6).

The white arrows in figure S2a identify example enhancements in SKR flux density with associated low frequency extensions (LFE) and a right-hand circular polarisation (northern hemisphere emission), for example, at 0800 UT on 29 September, 1200 UT on 05 October and 2000 UT on 06 October. These occur at, or near, the expected phase for northern hemisphere emissions and are characteristic of internally-triggered SKR enhancements that are controlled by magnetospheric rotational modulation[7]. The physical significance of these LFEs has been linked to increased precipitation of particles into the auroral zone and growth/movement of the radio source to higher altitudes (and hence lower frequencies since the emission frequency is inversely proportional to magnetic field strength).

Following these LFEs there are two long-lasting enhancements in SKR power on 08 October for 15 hours and 11 October for 24 hours, more characteristic of external solar wind control[4]. During these periods SKR is a very strong emission that lasts for more than one Saturn rotation, and does not have any correlation with northern or southern SKR phase[6]. The low frequency range (<10 kHz) displays intense SKR. The disappearance of SKR emissions around 2300 UT on 12 October is due to the spacecraft reaching Saturn periapsis (e.g., Figure S3) where SKR is not visible. The detached nature of the low

© 2015 Macmillan Publishers Limited. All rights reserved

frequency SKR emissions may be produced by a spatially separated (in longitude or latitude) source region with different regions producing the high- and low-frequency emissions. The direction-finding capabilities of the RPWS instrument allow us to investigate if the source region was spatially separated but unfortunately the spatial resolution of the analysis was not sufficient due to the distance of Cassini from Saturn. A more likely interpretation is that the gap is due to refractive effects from the propagation of the emissions through the complex plasma environment of Saturn's inner magnetosphere. Similar refractive effects are observed at Earth as auroral kilometric radiation propagates through Earth's plasmasphere. This interpretation is supported by the abrupt change in SKR polarisation near 70-80 kHz which is difficult to incorporate in a description involving spatially separated sources.

The first event originates from the northern hemisphere (right-hand circular polarisation) and the second from the southern hemisphere (left-hand circular polarisation). If these were the same event, but viewed from the northern, then the southern hemisphere, we might expect to see a change in polarisation at the equator. However, the northern hemisphere emission fades well before the spacecraft crosses the equator, and at a point where the latitude and local time are varying slowly. Furthermore, the near-equatorial spacecraft location during these two events implies that the emissions are not fading due to the spacecraft passing into a region where they are no longer visible[2]. Hence, this is evidence for two periods of long-lasting SKR enhancement that are driven separately by external large-scale compressions of the magnetosphere. Therefore we associate these two periods of strong SKR emissions with external compressions of the magnetosphere. We shifted the ENLIL time-series by 5.3 days such that the first major SKR enhancement begins at the arrival of the first large pressure pulse in the ENLIL time-series. This was done by matching the rise in dynamic pressure with the rise in intensity of SKR emissions.

© 2015 Macmillan Publishers Limited. All rights reserved

 DOI: 10.1038/NPHYS3565

Given the ~10 hour lag between the arrival of a solar wind dynamic pressure front and the increase in SKR emissions[5] we assign an uncertainty of 0.5 days to this estimate (4.8-5.3 days). In doing this, the second strong enhancement in SKR flux density matches the second pressure pulse in the ENLIL results thus providing supporting evidence that these enhancements in SKR are associated with externally-driven magnetospheric compressions. We also note that the increase in solar wind dynamic pressure occurs at the forward shock (FS) and occurs approximately at the same time as the onset of the periodic LFEs and the onset of this activity might represent the arrival of the CIR at Saturn.

Finally, the low frequency SKR emissions are accompanied by rising periodic narrow band emissions, mainly with opposite polarisation. These appear at frequencies around 5 kHz, so-called Saturnian Myriametric Radiation or n-SMR (*8*) and around 20 kHz, identified as narrowband SKR or n-SKR[2]. n-SMR are similar to continuum emissions from Earth's plasmapause, and n-KOM emissions from the Io torus, which are known to be generated at density gradients[8]. These might be attributed to dynamics internal to the plasma disc but in this case there is evidence that they are triggered by increases in the solar wind dynamic pressure. Although the spacecraft is moving latitudinally, there is no correlation of the morphology of the emissions with the location of the spacecraft, and the emissions appear after the major magnetospheric compressions (figure S2g). Activity in n-SKR and n-SMR continues however until 17 October, which is a much longer period than the 4 – 5 days previously reported[8] and may reflect the strength of the external compression, or that the initial external trigger has resulted in a “cascade” of internally-driven responses.

In summary, shifting the ENLIL time series by 4.8-5.3 days (to form the shifted time series in figure S2) we arrive at the following sequence of upstream events. Between 0000 UT and 1200 UT on 06 October a forward shock impacted Saturn and over the course of ~12 hours the magnetosphere was slowly compressed from a subsolar magnetopause position

© 2015 Macmillan Publishers Limited. All rights reserved

of 25 R_S to 17 R_S representing a moderate compression due to the enhanced compressibility of Saturn's magnetosphere compared to Earth[9]. A pressure pulse with a peak dynamic pressure of 0.23 nPa arrives between 1200 UT on 07 October and 0000 UT on 08 October compressing the magnetosphere over the next ~6 hours such that the magnetopause subsolar distance decreases to 14±2 R_S, representing an extreme and relatively rare compression. The pressure pulse begins to fade around 16 hours after it arrived falling back to a magnetopause subsolar distance of ~20 R_S by the end of 08 October. Between the middle of the day on 09 October and early on 10 October a smaller pressure pulse arrives producing a magnetopause standoff distance of 16±2 R_S.

Rotation of the magnetic field data to remove the effect of sweepback

The magnetic field at Saturn is swept-back into a lagging configuration over most local times produced by a combination of magnetopause currents and outward transport of internally produced plasma[10], although the latter is thought to dominate the observed sweep-back. The effect of this sweep-back is to introduce an azimuthal component to the magnetic field (in spherical polar coordinates) which reverses in sense about the centre of the current sheet such that the azimuthal and radial components of the field have an anti-phase relationship. Typically, $B_r>0$ and $B_\varphi<0$ above the current sheet, and $B_r<0$ and $B_\varphi>0$ below the current sheet. In collisionless reconnection, separation of ions and electrons occurs as the ions demagnetise in the ion diffusion region but where the electrons remain frozen to the field and continue to inflow towards the X-line where they eventually demagnetise at the electron scale. This separation of ions and electrons produces a current system known as the Hall current and associated field (the Hall magnetic field)[11]. There is also a Hall electric field associated with this structure, but in this article we will

© 2015 Macmillan Publishers Limited. All rights reserved

 DOI: 10.1038/NPHYS3565

refer to the Hall magnetic field as simply the Hall field. The Hall field has a quadrupolar structure with out-of-plane components.

Figure S4 illustrates the relationship between the Hall field and the azimuthal field associated with sweep-back and highlights the fact that the presence of the Hall field may be masked by the swept-back configuration of the field. For example, on the tailward side of the X-line the Hall field has a positive out-of-plane component above the current sheet but the swept-back configuration also produces a positive out-of-plane component. Hence, in the KRTP coordinate system it is hard to detect the presence of the Hall field. To clearly identify the Hall field we rotate the magnetic field data into an X-line coordinate system using the sweep-back angle of the field, defined as $\alpha=\tan^{-1}(B_\varphi/B_r)$:

$$\begin{pmatrix} B_x \\ B_y \\ B_z \end{pmatrix} = \begin{pmatrix} \cos\alpha & 0 & \sin\alpha \\ -\sin\alpha & 0 & \cos\alpha \\ 0 & -1 & 0 \end{pmatrix} \begin{pmatrix} B_r \\ B_\theta \\ B_\varphi \end{pmatrix} \qquad 1$$

This produces an X-line coordinate system where X points approximately tailward, Z points approximately northward, and Y completes the right-handed set pointing approximately dawnward. In the X-line frame the Hall field has components $B_H(x,z)$ in the y direction which when rotated by the sweep-back angle has components $(B_{Hr}, B_{H\theta}, B_{H\varphi}) = (-B_H \sin\alpha, 0, B_H \cos\alpha)$. Hence, adding the fields due to azimuthal and radial currents we find, $\mathbf{B}(B_r, B_\theta, B_\varphi) = \left\{B_{r0} \tanh\frac{-z}{D} - B_H \sin\alpha, B_{\theta 0}, B_{\varphi 0} \tanh\frac{-z}{D} + B_H \cos\alpha\right\}$ where we have simply modelled the radial and azimuthal currents with Harris current sheets. Applying this to our transformation (eq. 1) we obtain:

© 2015 Macmillan Publishers Limited. All rights reserved

$$\begin{pmatrix} B_x \\ B_y \\ B_z \end{pmatrix} = \begin{pmatrix} \cos\alpha & 0 & \sin\alpha \\ -\sin\alpha & 0 & \cos\alpha \\ 0 & -1 & 0 \end{pmatrix} \begin{pmatrix} B_{r0}\tanh\frac{-z}{D} - B_H \sin\alpha \\ B_{\theta 0} \\ B_{\varphi 0}\tanh\frac{-z}{D} + B_H\cos\alpha \end{pmatrix} \tag{2}$$

$$\begin{pmatrix} B_x \\ B_y \\ B_z \end{pmatrix} = \begin{pmatrix} B_{r0}\tanh\frac{-z}{D}\cos\alpha - B_H\sin\alpha\cos\alpha + B_{\varphi 0}\tanh\frac{-z}{D}\sin\alpha + B_H\sin\alpha\cos\alpha \\ -B_{r0}\tanh\frac{-z}{D}\sin\alpha + B_H\sin\alpha\sin\alpha + B_{\varphi 0}\tanh\frac{-z}{D}\cos\alpha + B_H\cos\alpha\cos\alpha \\ -B_{\theta 0} \end{pmatrix} \tag{3}$$

which simplifies to:

$$\begin{pmatrix} B_x \\ B_y \\ B_z \end{pmatrix} = \begin{pmatrix} B_{r0}\tanh\frac{-z}{D}\cos\alpha + B_{\varphi 0}\tanh\frac{-z}{D}\sin\alpha \\ -B_{r0}\tanh\frac{-z}{D}\sin\alpha + B_{\varphi 0}\tanh\frac{-z}{D}\cos\alpha + B_H \\ -B_{\theta 0} \end{pmatrix} \tag{4}$$

Finally, we note that $\alpha=\tan^{-1}(B_\varphi/B_r)$ and hence B_{r0} tanh(-z/D) sin(α) = $B_{\varphi 0}$ tanh(-z/D) cos(α) so

$$\begin{pmatrix} B_x \\ B_y \\ B_z \end{pmatrix} = \begin{pmatrix} B_{r0}\tanh\frac{-z}{D}\cos\alpha + B_{\varphi 0}\tanh\frac{-z}{D}\sin\alpha \\ B_H \\ -B_{\theta 0} \end{pmatrix} \tag{5}$$

Hence, the Hall field is obtained from the B_y component of the X-line coordinate system.

The sweep-back angle was measured from the magnetometer data between 08 Oct 2006 0000 UT and 0100 UT and found to be equal to -25.87º±4.87º and so a value of -26º was adopted in this study.

Electron pitch angle distributions near the X-line

Figure S5 shows reconstructed pitch angle distributions (PAD) in each quadrant of the X-line. CAPS/ELS has an instantaneous FOV of 160º×5.2º which is increased to ~160º×200º by a mechanical scanning platform. Each PAD is produced by combining fluxes measured over a single mechanical ~3 minute scan (actuation). Within this period ELS captures

© 2015 Macmillan Publishers Limited. All rights reserved

 DOI: 10.1038/NPHYS3565

spectra at a cadence between 2 and 32 s but for this study the maximum sampling time was restricted to 8s to avoid undetectable aliasing of the PAD. These fluxes were background-subtracted and sorted into 10º wide pitch angle bins and shifted by the (positive) spacecraft potential to remove trapped spacecraft photoelectrons. The raw spectrograms and reconstructed PADs were checked for evidence of aliasing.

In general the PAD is incomplete due to the limited field of view of the instrument. However, four typical PADs were identified in each quadrant of the X-line. Electron PADs in ion diffusion regions in Earth's magnetotail were found to consist of cool ~100 eV electrons flowing towards the X-line carrying the Hall current, and hotter >1 keV electrons flowing away from the X-line associated with acceleration near the X-line[12]. In Figure S5 we can see that due to the restricted field of view, the orientation of the spacecraft, and changes in orientation of the magnetic field, only electrons flowing out of the X-line are visible on the tailward side of the X-line, and electrons flowing towards the X-line are visible on the planetward side of the X-line. The samples in figure S5 were captured at 0242 UT (above the current sheet and tailward), 0341 UT (below and tailward), 0431 UT (below and planetward). We can see that the electrons flowing into the X-line are relatively cool with a peak energy near ~400 eV. The electrons flowing out of the X-line are hot about ~2 keV above the current sheet earlier in the interval at 0242 UT, and ~>10 keV below the current sheet later at 0341 UT. These are entirely consistent with hot electrons flowing out of the X-line and cooler electrons flow in towards the X-line and carrying the Hall current, similar to terrestrial observations[12].

Ion flows before and during the ion diffusion region encounter

Ion flows throughout the interval are difficult to analyse due to a combination of spacecraft rolls, limited viewing, low signal to noise and aliasing of the distributions. Figure S6 shows

© 2015 Macmillan Publishers Limited. All rights reserved

a time-energy spectrogram of ion fluxes measured by CAPS/IMS, with the electron fluxes and magnetic field for reference. In this figure ion fluxes have been summed over a 32s internal duty cycle of the instrument (an A-cycle) to improve the signal-to-noise and visibility of ion beams as the instrument actuates across the sky – thus relatively narrow ion beams appear as sharp gradients in the time-energy spectrogram. The “pulsing” in the background is correlated with the actuating motion of CAPS and is thought to be produced by a combination of CAPS actuating through a spatially asymmetrical background produced by radiation from Cassini’s radioisotope thermoelectric generators, and changes in the shielding of CAPS from this radiation as it actuates relative to the spacecraft platform and other instruments.

In figure S6 the ion fluxes for particular time intervals are presented as a function of look direction around the spacecraft in order to identify the flow direction of the ions. They also enable us to identify what directions about the spacecraft are not visible to the CAPS detector. These are presented in OAS coordinates in a polar projection. The OAS coordinate system is a spacecraft-centred frame where **S** is a vector from the spacecraft to the planet, **O** is a vector which is obtained from **S**×(**Ω**×**S**) and **A** is a vector along **S**×**O** and completes the right-handed set. The panels in figure S7 are presented in polar coordinates where the polar angle θ_{OAS} is the angle between a look vector and **S** such that $\theta_{OAS}=0^\circ$ represents a direction towards Saturn from Cassini, whereas 90º is perpendicular to the Cassini-Saturn line. The azimuthal angle φ_{OAS} is an angle around the **S**. Thus, each panel in figure S7 is drawn from the perspective of an observer on the spacecraft. The centre of the panel is looking at Saturn ($\theta_{OAS}=0^\circ$), the inner circle is $\theta_{OAS}=90^\circ$ and the outer circle $\theta_{OAS}=180^\circ$. Hence, ion fluxes in the inner circle are coming from “in front” of the spacecraft, and between the outer and inner circles come from “behind” the spacecraft. Fluxes from the left-hand side of the panel have a component of the flow in a prograde (corotational)

© 2015 Macmillan Publishers Limited. All rights reserved

 DOI: 10.1038/NPHYS3565

direction, and from the right-hand side have a component of the flow in an anti-corotational direction. Fluxes in the upper (lower) half of the panel are coming from above (below) and thus have a flow component directed downwards (upwards). The pink circle indicates the direction of the Sun and the pink square shows the direction of corotation.

The ion fluxes in S6 show significant fluxes from 2000 UT on 07 October to 0020 UT on 08 October with a decrease in flux from 2245 to 2330 UT which is correlated with a drop in the electron flux and an increase in the magnitudes of the B_r and B_φ components of the magnetic field and the magnetic field strength. Throughout this period the field of view of IMS covers close to the corotation direction and so this drop in flux is consistent with the motion of the spacecraft into the near-lobe – although a rotation of the flow to a more azimuthal direction and/or a narrowing of the ion beam (faster flows and/or colder ions) cannot be ruled out. Figure S7a shows the ion flow directions from 20:08:18 to 20:11:45 on 07 October and although CAPS does not fully capture the corotation direction, the flows are generally corotational. The ion distributions show clear evidence of two energy peaks, centred on ~300 eV/e and ~4000 eV/q, associated with H^+ and W^+ respectively, where the ratio in counts W^+/H^+= 0.72±0.06 from a fit to CAPS/IMS time-of-flight data.

From 0242 to 0251 UT energetic ion fluxes are observed, coincident with Cassini entering the northern part of the plasma sheet from the near lobe-regions. Figures S7b-S7d show the directions of these fluxes. Although the fluxes are very weak, close to the signal-to-noise threshold of IMS, the flow direction can be determined. At 0242-0245 (S7b) the ions are flowing in a tailward and slightly anti-corotational direction, then appear to be flowing tailward and slightly northward (S7c/S7d). The weakening in the fluxes in S7d is caused by the ions increasing to higher energies (as can be seen in figure S6). Generally, the typical ion energy is above ~2 keV/q and extends to the upper energy/charge range of the instrument. From the time-energy spectra there is some evidence in the beam in S7c for

© 2015 Macmillan Publishers Limited. All rights reserved

two ion peaks, one at ~8 keV/q and another at ~20 keV/q. From an analysis of the time-of-flight data, the 8 keV/q beam is associated with H^+ and the 20 keV/q beam with a species with mass/charge 2 (either He^{++} or H_2^+). An 8 keV/q H^+ ion has a flow speed of 1200 km s^{-1}. This is probably an upper limit to the speed due to the peak energy being due to a combination of bulk and thermal kinetic energy. The ratio of the mass/charge=2 counts to H^+ is 7±1. There are no W^+ ions to within the error of the analysis, although a W^+ ion moving at 1200 km s^{-1} has an energy/charge of 130 keV/q, well above the range of the CAPS/IMS sensor. The energetic ion detectors on Cassini are not orientated in a favourable direction to observe these ions at this time.

The energy spectrum associated with S7d is found about 10 keV/q, which corresponds to a speed of <=1400 km s^{-1}. Over the period in the region tailward of the X-line (0146-0355) the CAPS FOV is close to corotation (within ~10-20º) but no measurable fluxes are found in that direction.

From 0354 to 0825 UT the spacecraft undergoes continuous rolling, with another small roll from 0940 to 1000 UT. Due to this rolling behaviour IMS scans rapidly across the sky and it is very difficult to determine the flow directions of the ions. Very narrow features are found in anodes 6/7 at 0401 UT and anodes 1/2 at 0410 UT but these are not visible in OAS plots. This large-scale flow feature is consistent with the planetward-looking FOV and expected planetward reconnection exhaust jets. Evidence for corotational, but slightly tailwards flow is found from 0445 UT onwards, but only sporadic samples (S7e and S7f) are available due to the spacecraft roll. After 0500 UT the spacecraft samples the corotation direction very infrequently, but very low ion fluxes are expected due to the low plasma density, as indicated by the electron measurements[13].

© 2015 Macmillan Publishers Limited. All rights reserved

 DOI: 10.1038/NPHYS3565

Hence, these observations show that in the tailward region of the diffusion region (as determined from the magnetometer data) CAPS observes a $<\sim 1200$ km s^{-1} ion beam flowing tailward, as expected. By plotting the peaks in ion flux with the look direction information we can determine the flow directions in KSM coordinates and we find the following unit vectors for the three ion beams in figures S7b-S7d: (-0.95, -0.18, -0.27), (-0.77, 0.57, -0.30), and (-0.96, -0.077, -0.28) hence showing an ion beam directed tailward.

Flux ropes and secondary islands

Plasmoids, with a loop-like or fluxrope structure, are a common signature in planetary magnetotails[14,15] and can be found either travelling planetward or tailward. They can also be seen adjacent to an X-line as a "secondary island" produced as a result of instabilities that set in once reconnection has commenced[16], often in the presence of a significant guide field (perpendicular to the plane of the X-line). The signature of a plasmoid passing over the spacecraft is a bipolar feature in B_z with deflection in the B_x component in the X-line coordinate system.

The B_z component only changes sign if the spacecraft encounters both the leading and trailing hemispheres of the structure, and the B_x component only changes sign if the spacecraft encounters both the upper and lower hemispheres of the structure. Therefore, B_z and B_x will only have bipolar perturbations with no change in sign if the spacecraft encounters a single quadrant of the structure. Changes in sign will be introduced to these perturbations if additional quadrants are sampled. Thus in general we search for bipolar delta-Bz signatures and where the sense (positive-negative or negative-positive) of the perturbation can indicate the direction of motion. Signatures can still be detected if the spacecraft does not encounter the plasmoid but where the plasmoid is detected by the compression of the surrounding field as the plasmoid passes near the spacecraft. These

© 2015 Macmillan Publishers Limited. All rights reserved

are known as Travelling Compression Regions. If the plasmoid has an axial field then it is often termed a flux rope and B_y will show a maximum closest to the centre of the flux rope axis.

Figure S8 shows two periods in the tailward region of the X-line where loops have been identified by searching for these perturbations in B_z and B_x,. For clarity we only show loops where a negative excursion in B_z is observed. The heavy vertical lines show the passage of the loop. No evidence for flux rope-type signatures are found in these data.

The presence of loops close to the X-line is indicative of secondary islands. Although secondary islands can be found adjacent to the X-line in the diffusion region, they can also survive downstream, but in this scenario they provide a method to remote sense the diffusion region. At a minimum this then shows evidence for persistent ongoing reconnection.

Reconnection rate and Hall magnetic field strength

The ratio of the Hall magnetic field (B_y) to the field upstream of the current sheet (B_x) is a dimensionless estimate of the strength of the Hall field. Estimates of the dimensionless strength of the Hall field at Mars show peak values ranging between 0.29 and 0.76 but typically ~0.5 (15). These amplitudes were found to be comparable in size to the dimensionless amplitude of the Hall field at Earth with average values of 0.39±0.16 (17).

Similarly the ratio between the normal field (B_z) and the main field (B_x) is an estimate of the reconnection rate. For Mars, values ranging between 0.072 and 0.335 with an average of 0.16 and standard deviation of 0.09 have been reported, indicating that reconnection was in the regime of fast reconnection[17]. These values were slightly higher than at Earth but were perhaps the result of a bias towards intense events in the Mars data set.

© 2015 Macmillan Publishers Limited. All rights reserved

 DOI: 10.1038/NPHYS3565

Figure S9 shows estimates of the strength of the Hall field, $|B_y|/\max(|B_x|)$, and the reconnection rate $|B_z|/\max(|B_x|)$ for the diffusion region encounter described in this paper. The mean value of the Hall field (figure S9e) was 0.18±0.15, although the peak of 0.83 is much higher, compatible with the upper end of the published range[17,18]. The reconnection rate (figure S9f) was found to be 0.13±0.10 with a peak of 0.66 – hence demonstrating fast reconnection – and is similar to martian and terrestrial values.

Reconnection restart

Sporadically from 0605 UT and onward from 0640 UT on 08 October 2006 there is evidence that reconnection restarts or that a fresh part of the plasma sheet moves over the spacecraft and another X-line forms. The spacecraft is located in the southern extreme of the current sheet (steady $B_r<0$) and apparently on closed field lines (typically $B_\theta>0$). The plasma sheet electrons are hotter than typical[19], with energies between 300 eV and 1 keV.

Around 0610 UT a tailward moving loop is observed from a positive-negative bipolar signature in delta-B_θ (Figure 3) suggesting a reconnection X-line has formed planetward of the spacecraft. Since the B_θ perturbation doesn't go negative we interpret this as the remote detection of the loop and as such this is a Travelling Compression Region. From 0640 to 0700 UT hot electrons are observed with an energy of ~ 1 – 10 keV. At 0710 UT a dipolarisation front passes the spacecraft as noted by the peak in |**B**| and appearance of hot >1 keV electrons. Another front passes the spacecraft at ~0810 UT. These dipolarisation front passages are interspersed with intervals in the plasma sheet suggesting that a section of the plasma sheet tailward of the spacecraft is reconnecting and Cassini is sporadically immersed in the exhaust from that X-line. After the dipolarisation front at 0810 UT the spacecraft is immersed in hot electrons that increase in energy with time. Additional smaller-scale positive-negative bipolar B_θ structures are seen

© 2015 Macmillan Publishers Limited. All rights reserved

in this hot exhaust region suggesting the presence of multiple small-scale dipolarisation fronts[20].

Figure S10 shows ion and electron time-energy spectrograms during these dipolarisation fronts. As noted in section 6, from 0354 to 0825 UT the spacecraft is continuously rolling, with another small roll from 0940 to 1000 UT. Due to this rolling behaviour IMS scans rapidly across the sky and it is very difficult to determine the flow directions of the ions. No significant ion fluxes are observed during the passage of the tailward plasmoid at 0640 UT even though the IMS field-of-view is sufficient to observe tailward flows. During the dipolarisation front at 0710 UT the field-of-view could have seen inward flows from the dawn sector but not from the near-corotation direction.

Significant fluxes are observed between ~0730 and ~0800 UT. Figure S11 shows ion fluxes organised in OAS coordinates. Figures S11a and S11b show ion fluxes from the end of the energetic electron interval after the first dipolarisation front and the entry into the plasma sheet region around ~0730 UT. Figure S11a shows ion fluxes whilst still in the energetic electron region. The IMS field-of-view does not fully capture these ions but assuming IMS captures the edge of the ion beam they appear to be moving inwards and from the duskward direction. Figure S11b shows the next slice and where flows appear from the corotation direction. The nominal plasma sheet during this region has ratios of total counts of various species, $W^+/H^+=13\pm3$ and $(m/q=2)/H^+=12\pm1$, showing a plasma sheet dominated by heavy ions.

No significant ion fluxes are observed between 0800 UT and ~1100 UT, but the IMS viewing is biased to seeing outflows, hence this is not unexpected since the spacecraft is embedded in heated plasma on closed field lines and so we might expect inflows. Figure S12 shows the ion and electron fluxes for the remainder of the dynamical effects on 08

© 2015 Macmillan Publishers Limited. All rights reserved

 DOI: 10.1038/NPHYS3565

October. Ion fluxes as a function of the field-of-view are in figures S11c-S11i. At 1115 UT (figure S12c) ions >~5 keV/q (speed ~1000 km/s for H^+ ions) are observed moving northward, planetward and dawnward consistent with a location in this energised region on closed field lines connected to the exhaust from a reconnection site. Shortly after that (at ~1130) the spacecraft enters the plasma sheet with ~200 eV electrons and ions flowing in the corotation direction (and slightly upward) (figure S12d). The spacecraft re-enters the hot exhaust region around 1240 UT and no significant ion fluxes are seen until 1332 UT despite IMS seeing the whole sky due to spacecraft rolls – although the non-detection of ions might be a combination of flow energies exceeding the energy range of IMS and the flux of ions being below the sensitivity threshold for IMS[13]. At 1332 UT ions are seen just at the edge of the field of view of IMS and suggest inward flow possibly with a downward and dawnward component (figure S11e), again consistent with the location of the spacecraft in the hot exhaust region. Shortly after at 1336 UT the ion flows are more corotational but still with an inward component (figure S11f). Between ~1530 and 1730 the spacecraft is located in the southern lobe, and energetic electron boundary layers are seen near the boundary between the lobe and the plasma sheet. In the boundary layers, ions are found flowing along the magnetic field with pitch angles of 0º (figures S11g and S11h) towards the planet. These boundary layers are on closed field lines, as indicated by the presence of an energetic electron population flowing towards the planet with a pitch angle of 0º, with a counterstreaming component as far as can be seen in the antiparallel direction (figure S13). Finally, the interval ends with a return to the plasma sheet and corotational ion flow (figure S11i).

Supplementary Materials References

1. Odstrcil, D. Modeling 3D solar wind structure. *Adv. Space Res.* **32**, 497, 2003.

© 2015 Macmillan Publishers Limited. All rights reserved

2. Lamy, L. *et al.* Saturn kilometric radiation: Average and statistical properties. *J. Geophys. Res.* **113**, A07201, doi:10.1029/2007JA012900, 2008.

3. Jian, L. K. *et al.* Comparison of Observations at ACE and Ulysses with Enlil Model Results: Stream Interaction Regions During Carrington Rotations 2016 – 2018. *Solar Phys.* **273**, 179-203, doi:10.1007/s11207-011-9858-7, 2011.

4. Kurth, W. S. *et al.* Saturn kilometric radiation intensities during the Saturn auroral campaign of 2013. *Icarus*, in press, doi:10.1016/j.icarus.2015.01.003.

5. M. D. Desch & H. O. Rucker The relationship between Saturn kilometric radiation and the solar wind. *J. Geophys. Res.* **88**, pp. 8999-9006, doi:10.1029/JA088iA11p08999, 1983.

6. L. Lamy, Variability of southern and northern periodicities of Saturn Kilometric Radiation. Proc. 7th International Workshop on Planetary, Solar and Heliospheric Radio Emissions (PRE VII), Graz, Austria, September 15-17, 2010, pp. 38-50, 2011.

7. C. M. Jackman *et al.* On the character and distribution of lower-frequency radio emissions at Saturn and their relationship to substorm-like events. *J. Geophys. Res.* **114**, A08211, doi:10.1029/2008JA013997, 2009.

8. P. Louarn *et al.* Observation of similar radio signatures at Saturn and Jupiter: Implications for the magnetospheric dynamics. *Geophys. Res. Lett.* **34**, L20113, doi:10.1029/2007GL030368, 2007.

9. S. J. Kanani *et al.* A new form of Saturn's magnetopause using a dynamic pressure balance model, based on in situ, multi-instrument Cassini measurements. *J. Geophys. Res.* **115**, A06207, doi:10.1029/2009JA014262, 2010.

© 2015 Macmillan Publishers Limited. All rights reserved

10. C. S. Arridge *et al.* Mapping magnetospheric equatorial regions at Saturn from Cassini prime mission observations. *Space Sci. Rev.* **264**(1-4), pp. 1-83, doi:10.1007/s11214-011/9850-4, 2011.

11. Øieroset, M., Phan, T.D., Fujimoto, M., Lin, R.P., Lepping, R.P. In situ detection of collisionless reconnection in the Earth's magnetotail. *Nature* **412**, pp. 414-417 (2001).

12. Nagai, T. *et al.* Geotail observations of the Hall current system: Evidence of magnetic reconnection in the magnetotail. *J. Geophys. Res.* **106**, A11, pp. 25929-25949 (2001).

13. McAndrews, H.J. *et al.* Plasma in Saturn's nightside magnetosphere and the implications for global circulation. *Planet. Space Sci.* **57**, pp.1714-1722, doi:10.1016/j.pss.2009.03.003, 2009.

14. Eastwood, J. P. *et al.* Evidence for collisionless magnetic reconnection at Mars. *Geophys. Res. Lett.* **35**, L02106, doi:10.1029/2007GL032289 (2008).

15. Jackman, C.M. *et al.* Saturn's dynamic magnetotail: A comprehensive magnetic field and plasma survey of plasmoids and traveling compression regions and their role in global magnetospheric dynamics. *J. Geophys Res. Space Physics*, **119**, 5465-5495, doi:10.1002/2013JA019388 (2014).

16. Drake, F., Swisdak, M., Schoeffler, K.M., Rogers, B.N., Kobayashi, S. Formation of secondary islands during magnetic reconnection. *Geophys. Res. Lett.* **33**, L13105, doi:10.1029/2006GL025957, 2006.

17. Eastwood, J. P., Phan, T. D., Øieroset, M., Shay, M. A.. Average properties of the magnetic reconnection ion diffusion region in the Earth's magnetotail: The 2001-2005 Cluster observations and comparison with simulations. *J. Geophys. Res.* **115**, A08215, doi:10.1029/2009JA014962 (2010).

© 2015 Macmillan Publishers Limited. All rights reserved

18. Halekas, J. S. *et al.* In situ observations of reconnection Hall magnetic fields at Mars: Evidence for ion diffusion region encounters. *J. Geophys. Res.* **114**, A11204, doi:10.1029/2009JA014544 (2009).

19. Arridge, C. S. *et al.* Plasma electrons in Saturn's magnetotail: Structure, distribution and energisation. *Planet. Space Sci.* **57**, 2032-2047, doi:10.1016/j.pss.2009.09.007 (2009).

20. Chen, L.-J. *et al.* Observation of energetic electrons within magnetic islands. *Nature Physics* **4**, pp.19-23, doi:10.1038/nphys777, 2008.

Figures and captions

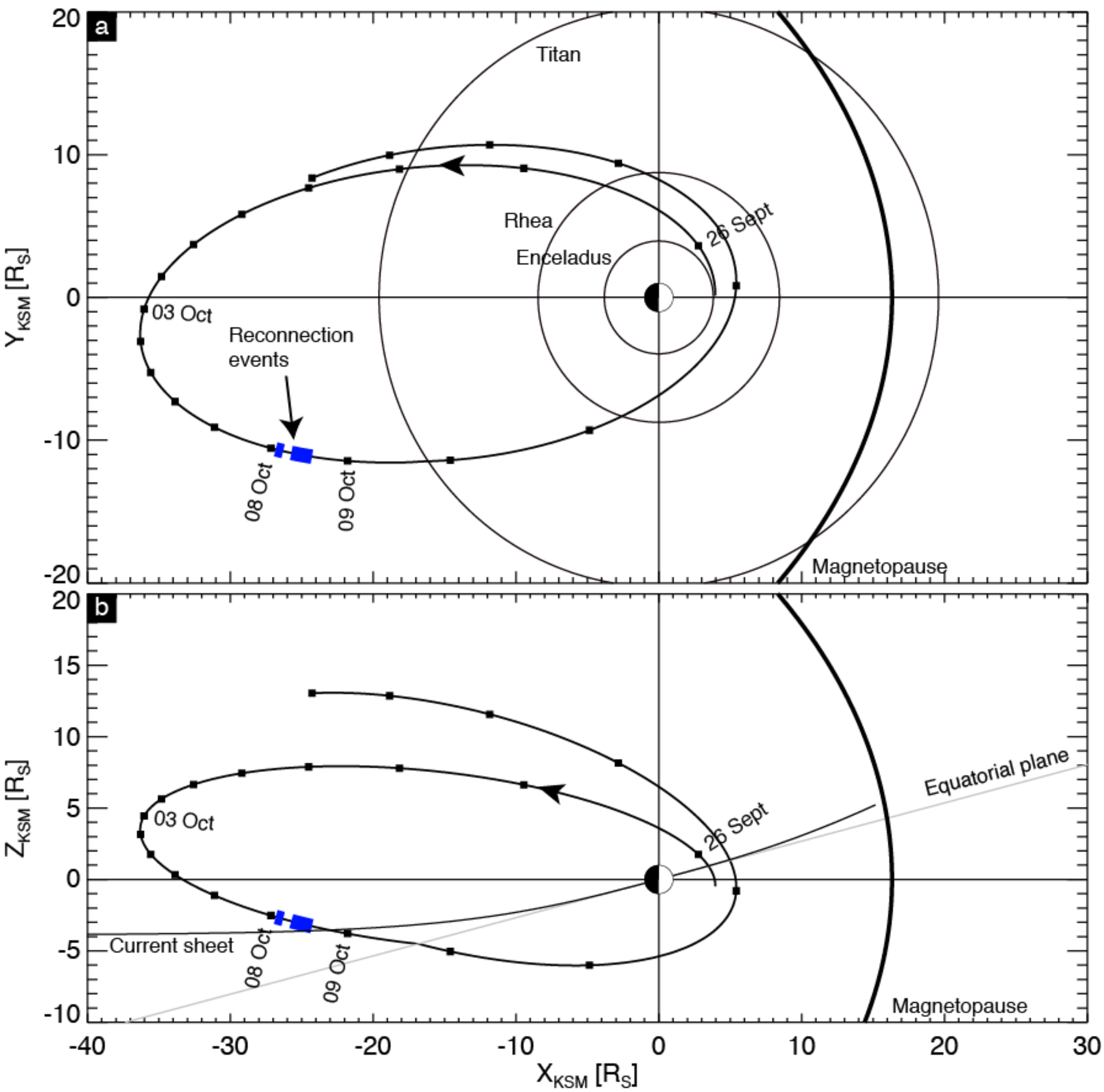

© 2015 Macmillan Publishers Limited. All rights reserved

DOI: 10.1038/NPHYS3565

Figure S1: Trajectory of Cassini in KSM during the event in this paper (highlighted in blue). Panel (a) shows the trajectory projected into the X-Y plane and (b) the X-Z plane. The model current sheet location is shown in panel (b) and a model magnetopause in both panels.

© 2015 Macmillan Publishers Limited. All rights reserved

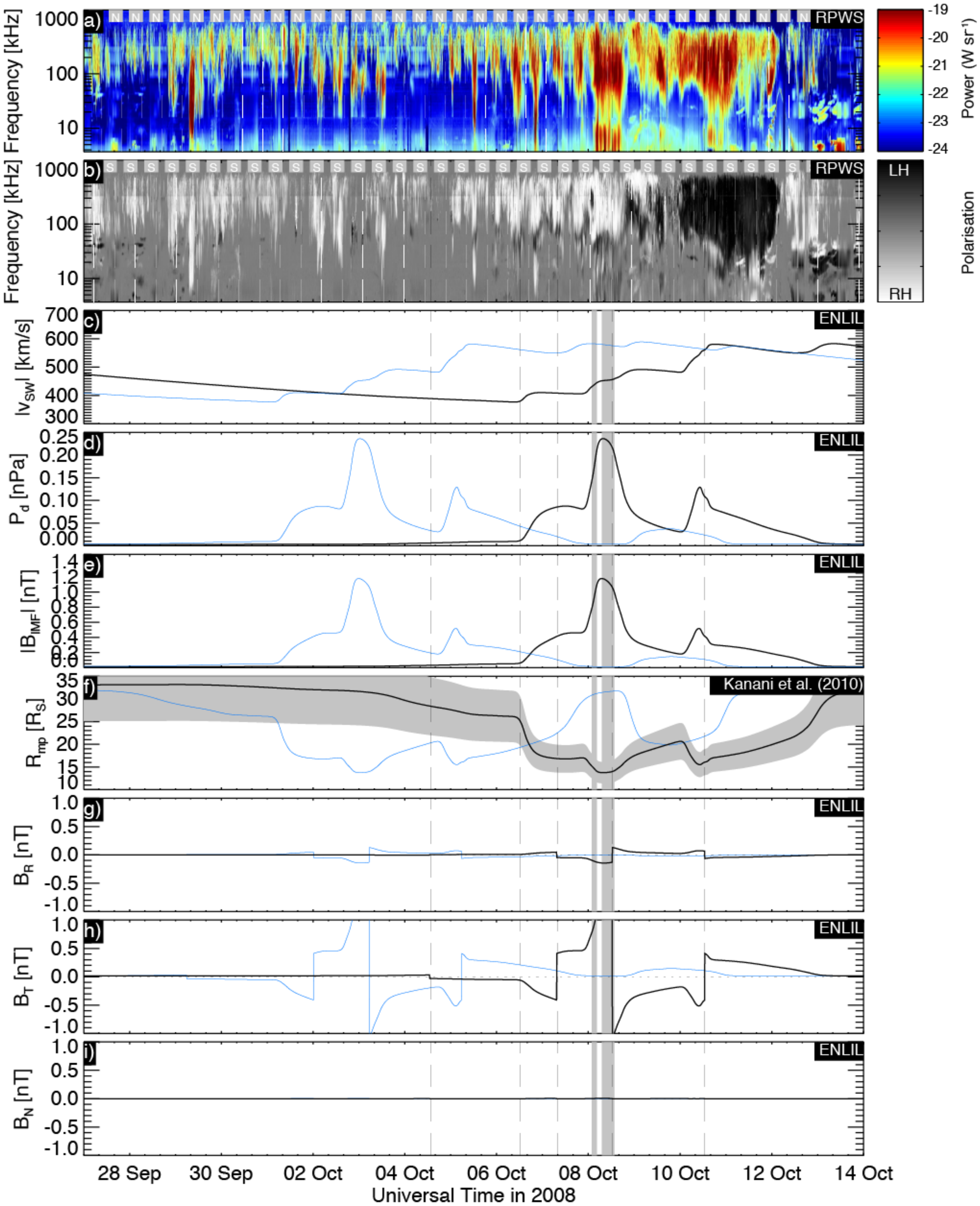

Figure S2: Cassini radio and plasma wave observations and ENLIL solar wind simulation results showing the inferred upstream solar wind conditions during the event: (a) electric field flux density measured by the Cassini/RPWS instrument and scaled to 1 AU distance,

© 2015 Macmillan Publishers Limited. All rights reserved

 DOI: 10.1038/NPHYS3565

grey “S” and white vertical lines indicates when SKR emissions from the southern hemisphere should be detected based on the SLS4 system; (b) electric field circular polarisation measured by the Cassini/RPWS instrument (white indicates emissions from the northern hemisphere, black from the south), grey and white vertical lines indicates when SKR emissions from the northern hemisphere should be detected based on the SLS4 system; (c) solar wind speed from ENLIL; (d) solar wind dynamic pressure from ENLIL; (e) interplanetary magnetic field strength from ENLIL; (f) inferred subsolar position of the magnetopause based on the ENLIL dynamic pressure and a model magnetopause[9]; (g-i) magnetic field in the RTN coordinate system from ENLIL. The vertical dashed black lines indicate HCS crossings. The grey vertical bars indicate the reconnection regions in Figure 3 of the main manuscript. In each ENLIL panel the blue curves show the original ENLIL data, black shows the ENLIL data which has been shifted in time by 5.3 days to match the enhancements in the measured SKR flux, as discussed in the Supplementary Material text.

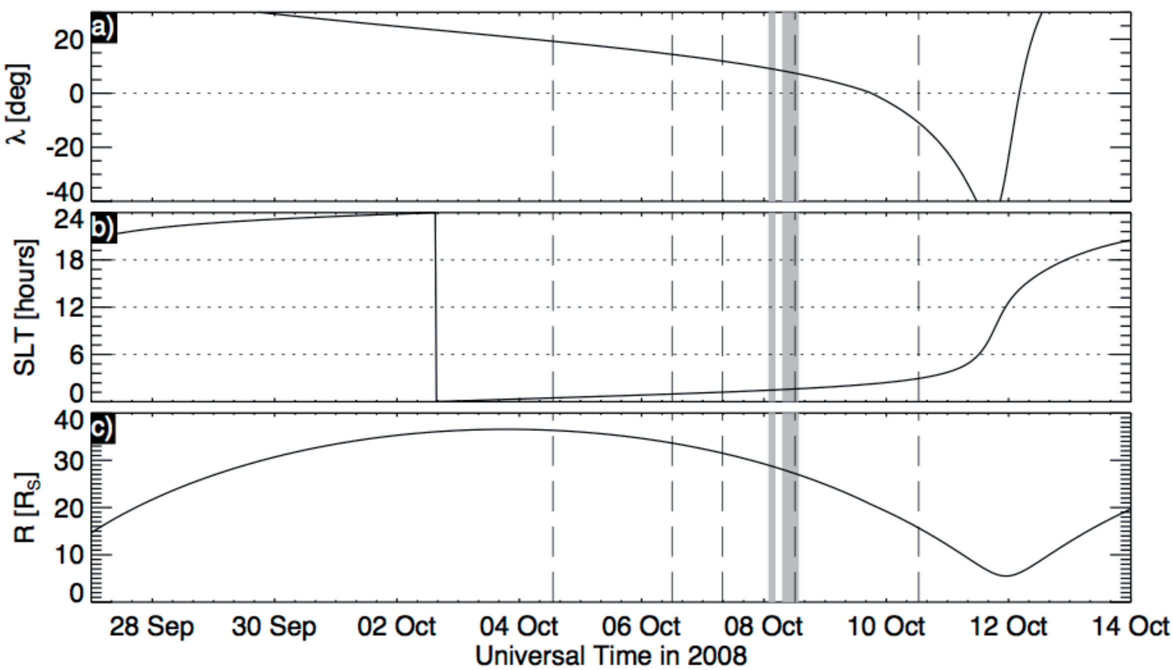

© 2015 Macmillan Publishers Limited. All rights reserved

Figure S3: Cassini orbital parameters used to interpret Cassini radio and plasma wave observations: (a) latitude, (b) local time and (c) radial distance of Cassini.

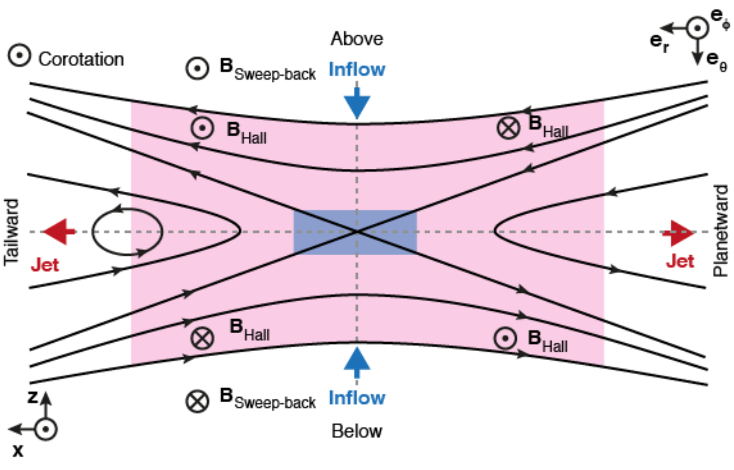

Figure S4: Schematic diagram showing the reconnecting current sheet with the ion (pink) and electron (blue) diffusion regions[11], inflow and outflow jets, and the orientation of the Hall magnetic field and magnetic field associated with the sweep-back of the magnetic field.

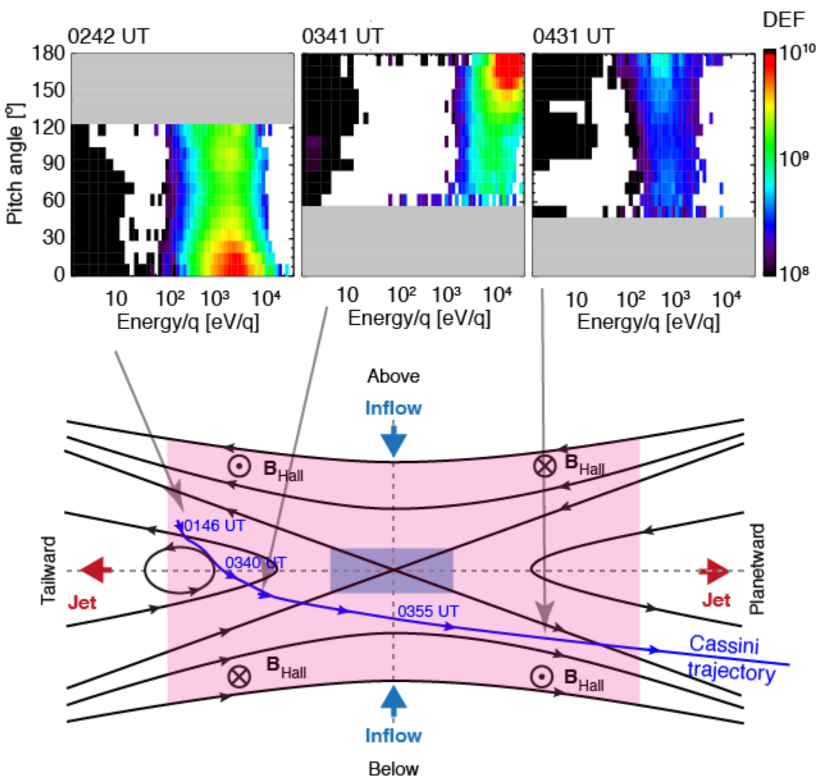

© 2015 Macmillan Publishers Limited. All rights reserved

DOI: 10.1038/NPHYS3565

Figure S5: Electron pitch angle distributions in three of the four quadrants of the X-line. Because of changes in orientation of the spacecraft and the magnetic field, combined with the 160º×5º instantaneous field of view of the ELS analyser, the pitch angle coverage is generally incomplete with pitch angles of only 0º or 180º covered by the instrument field of view. The colour scale shows the measured differential energy flux in units of eV m^{-2} s^{-1} sr^{-1} eV^{-1}.

© 2015 Macmillan Publishers Limited. All rights reserved

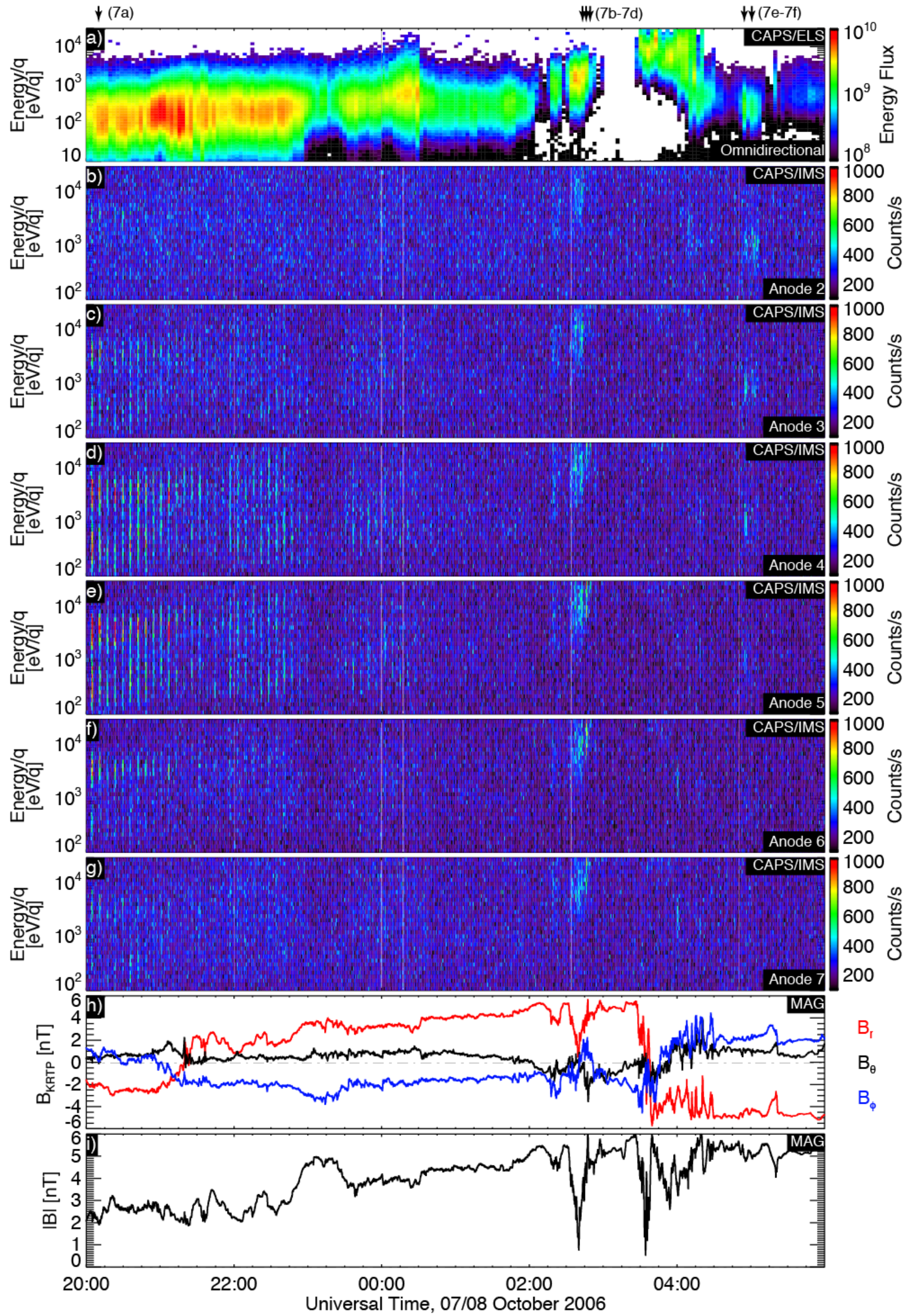

541

© 2015 Macmillan Publishers Limited. All rights reserved

 DOI: 10.1038/NPHYS3565

Figure S6: Ion fluxes measured by CAPS/IMS with electron fluxes and magnetic field data for reference. Panels (b-g) show ion fluxes from anodes 2-7 of CAPS/IMS on a linear colour scale from 100 to 1000 counts/32s (summed over a 32s instrument duty cycle). There are no measurable fluxes below 100 eV/q. The arrows at the top of each panel indicate the times of the OAS plots presented in figure S7.

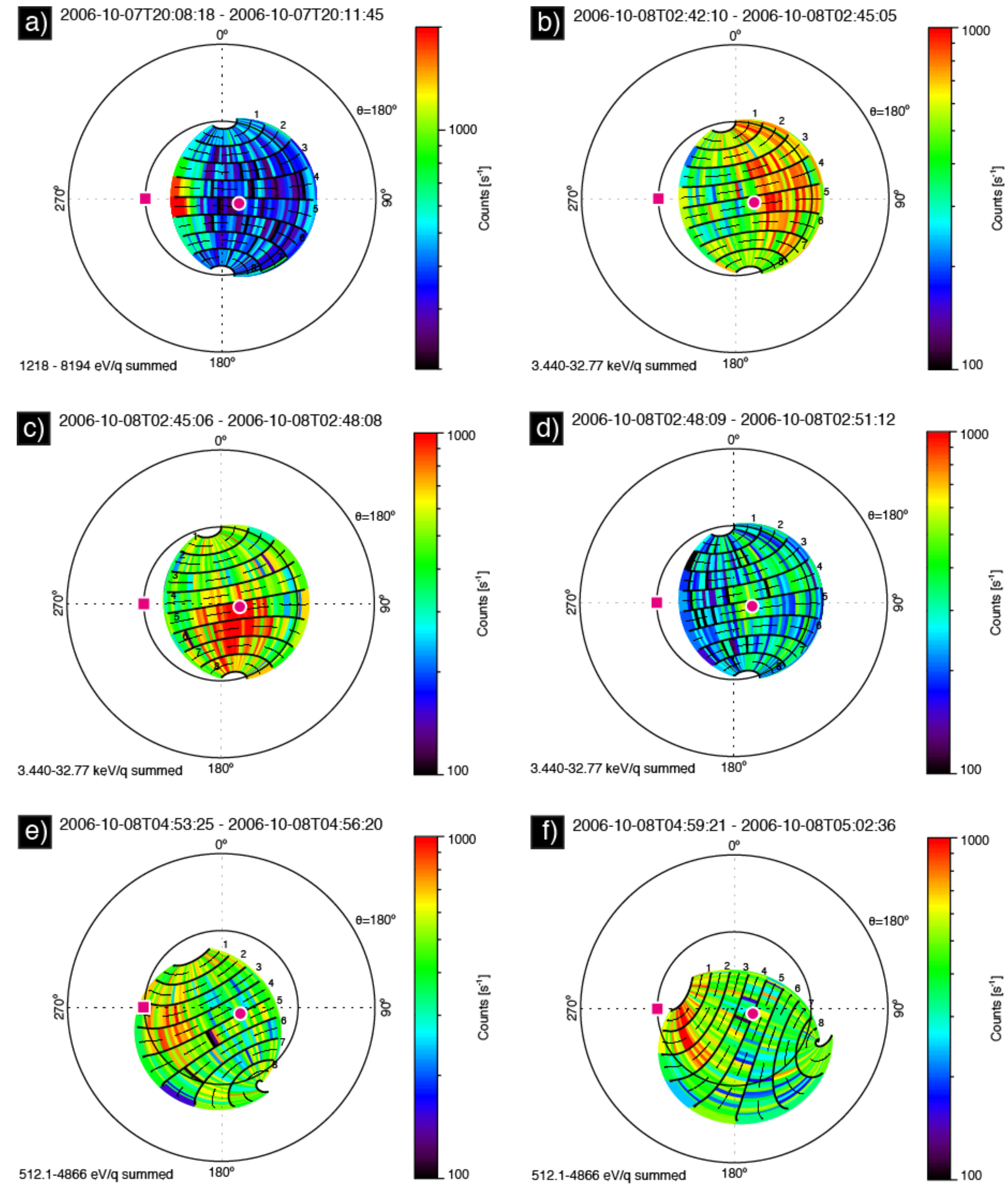

© 2015 Macmillan Publishers Limited. All rights reserved

Figure S7: Ion fluxes presented as a function of look direction in OAS coordinates. .Pink circles show the Sun direction, and pink square shows the corotation direction. Saturn is in the centre of each panel.

© 2015 Macmillan Publishers Limited. All rights reserved

 DOI: 10.1038/NPHYS3565

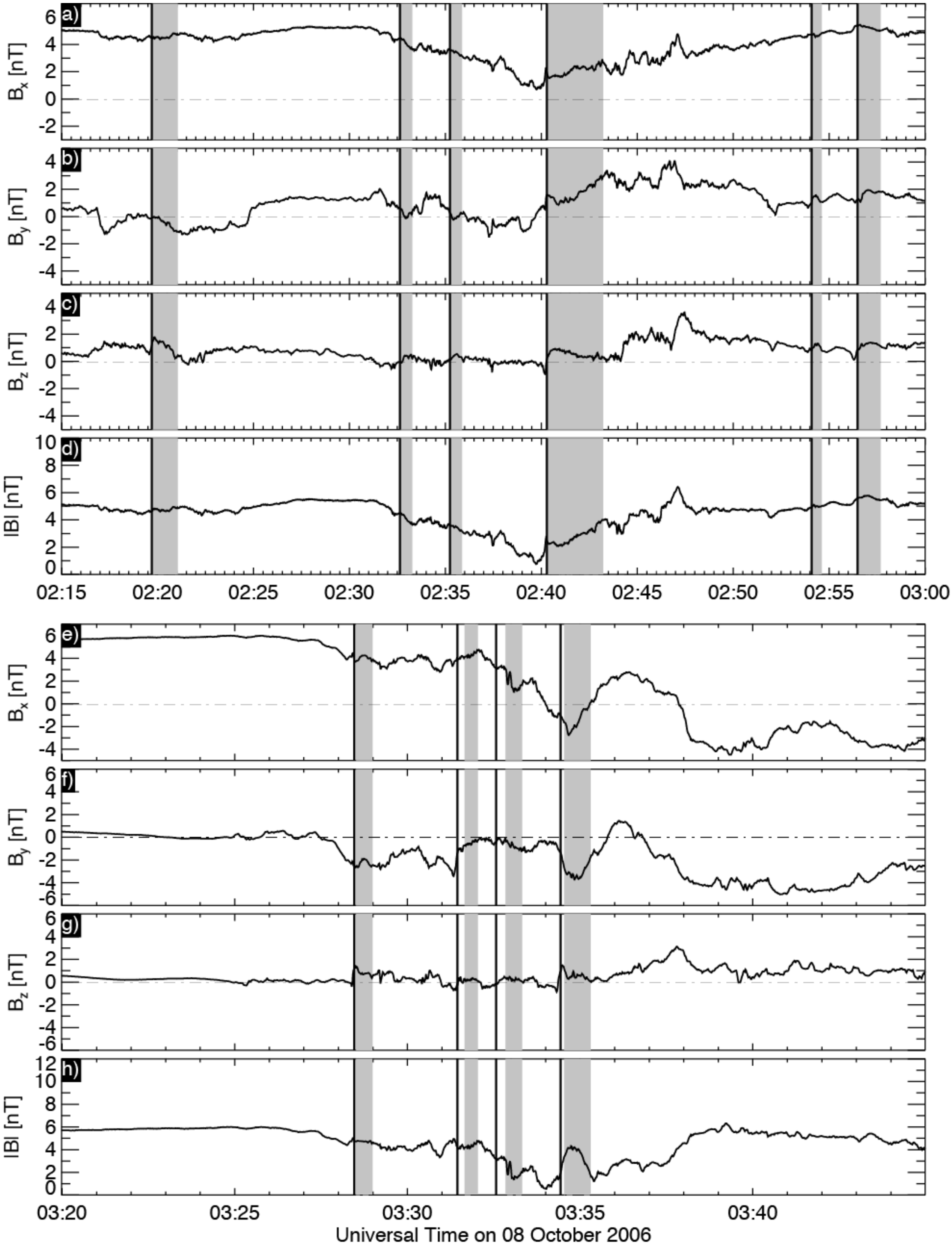

Figure S8: Small plasmoids observed in magnetometer data on the tailward side of the X-line. Panels (a-d) show magnetometer data from 0215 – 0300 UT and panels (e-h) show

© 2015 Macmillan Publishers Limited. All rights reserved

data from 0320-0345 UT on 08 October. Both sets of data are presented in the X-line coordinate system. The bold vertical lines indicate the passage of small plasmoids, the shaded grey regions indicate post-plasmoid plasma sheets. Note the different time scales and y-axis scales in each plot.

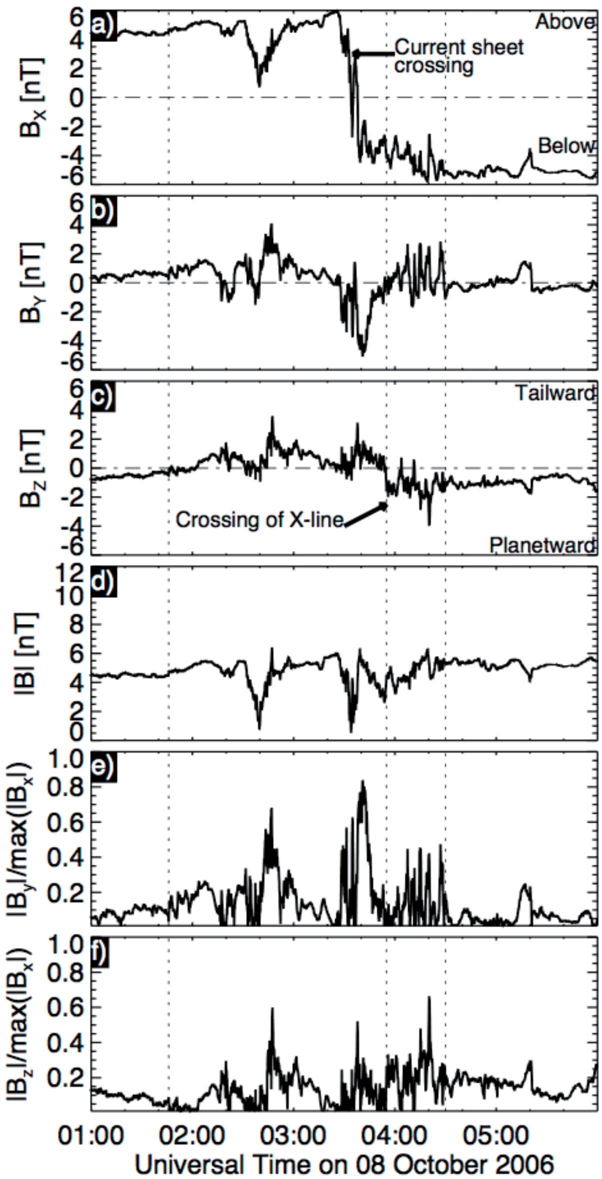

Figure S9: Reconnection rate and Hall magnetic field strength estimates near the diffusion region. Panels (a-d) show the measured magnetic field in the X-line coordinate system, panel (e) shows the strength of the Hall field expressed as the dimensionless ratio

© 2015 Macmillan Publishers Limited. All rights reserved

 DOI: 10.1038/NPHYS3565

$|B_y|/\max(|B_x|)$ and panel (f) shows a dimensionless proxy for the rate of reconnection given by as the dimensionless ratio $|B_z|/\max(|B_x|)$.

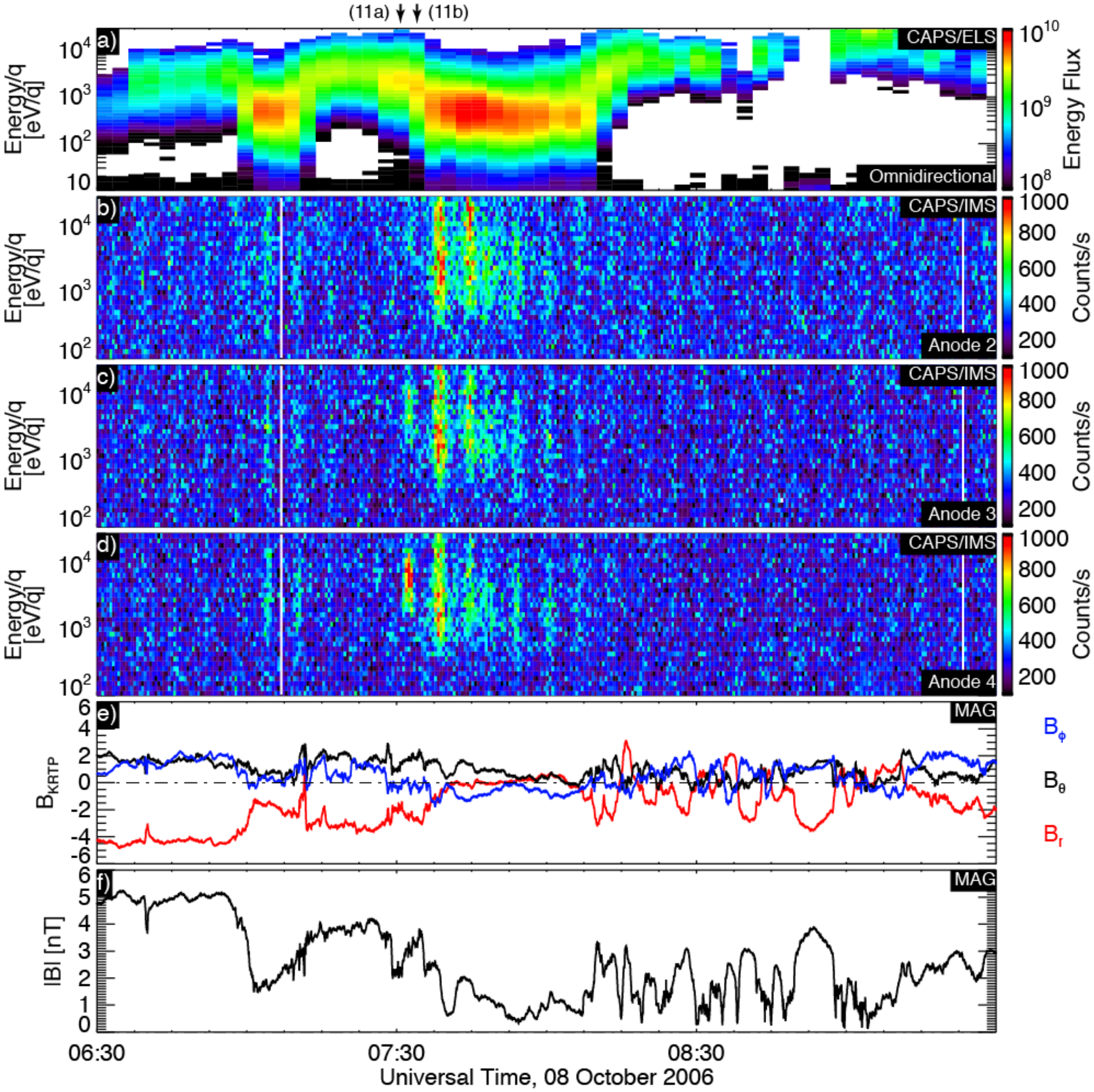

Figure S10: Electron, ion and magnetic field observations during re-encounter or restart of reconnection. Panel (a) shows a CAPS/ELS time-energy spectrogram of omni-directional flux averaged over a CAPS actuation cycle. Panels (b-d) show time-energy spectrograms of ion flux averaged over 32s from anodes 2-4 of CAPS/IMS (the anodes showing the highest flux). Panels (e) and (f) show the magnetic field components and field magnitude.

© 2015 Macmillan Publishers Limited. All rights reserved

The arrows at the top of each panel indicate the times of the OAS plots presented in figure S11.

© 2015 Macmillan Publishers Limited. All rights reserved

DOI: 10.1038/NPHYS3565

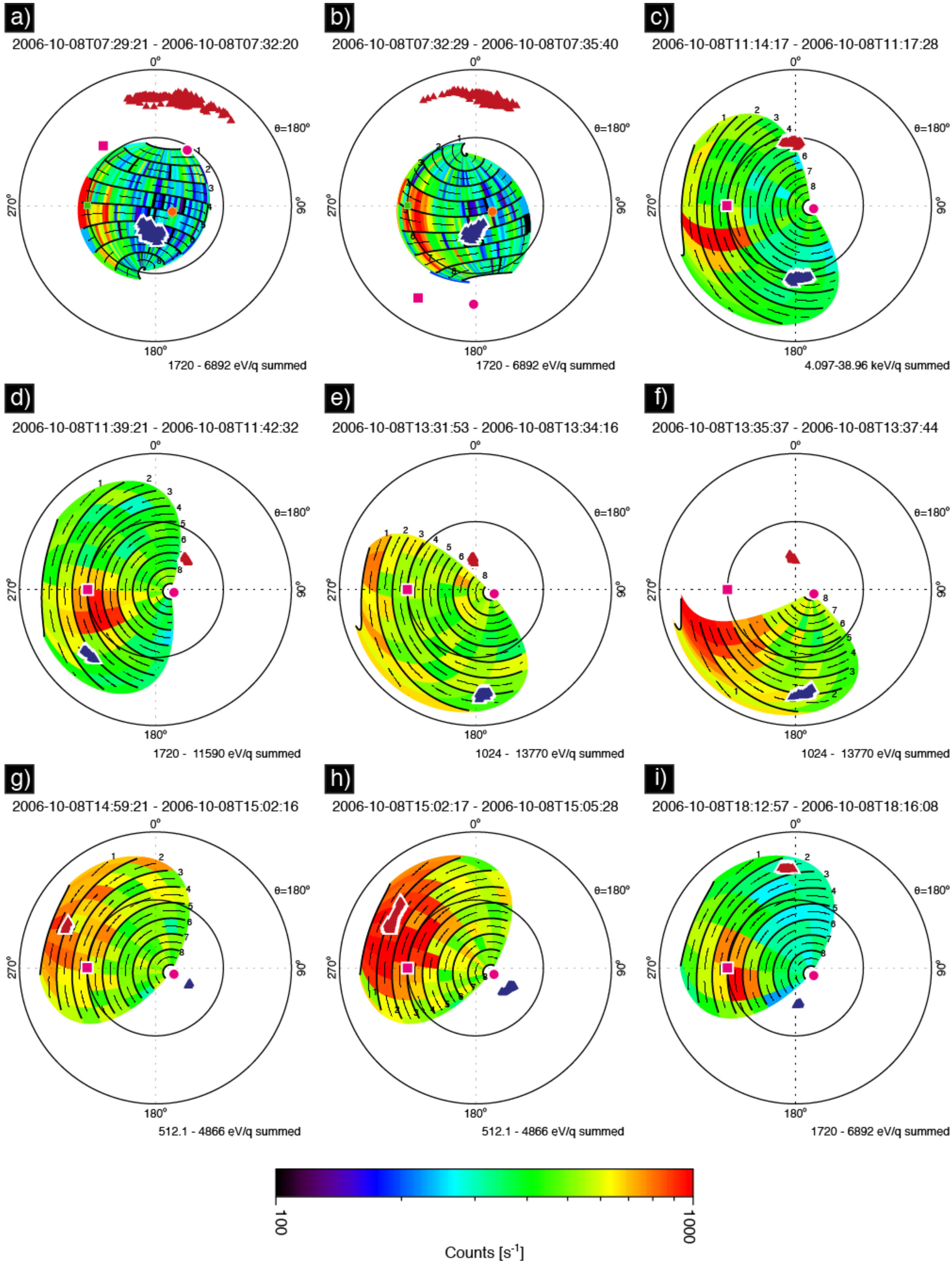

572

© 2015 Macmillan Publishers Limited. All rights reserved

Figure S11: Ion fluxes presented as a function of look direction in OAS coordinates corresponding to times in figures S10 and S12. Red and blue triangles show 0º and 180º pitch angle directions respectively. Pink circles and squares show the directions to the Sun and corotation direction respectively. Saturn is in the centre of each panel.

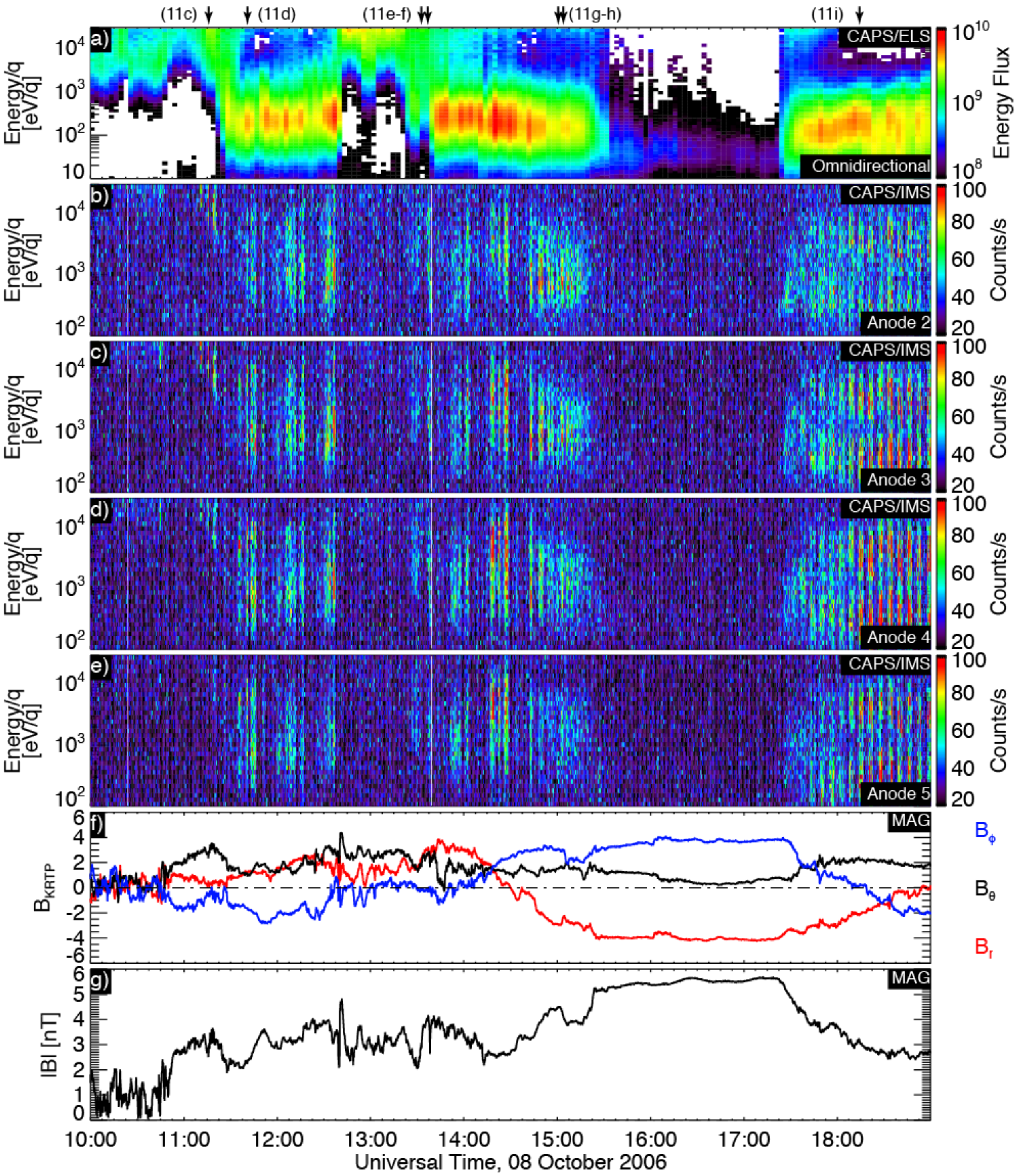

© 2015 Macmillan Publishers Limited. All rights reserved

 DOI: 10.1038/NPHYS3565

Figure S12: Electron, ion and magnetic field observations during re-encounter or restart of reconnection. Panel (a) shows a CAPS/ELS time-energy spectrogram of omni-directional flux averaged over a CAPS actuation cycle. Panels (b-e) show time-energy spectrograms of ion flux averaged over 32s from anodes 2-5 of CAPS/IMS (the anodes showing the highest flux). Panels (f) and (g) show the magnetic field components and field magnitude. The arrows at the top of each panel indicate the times of the OAS plots presented in figure S11.

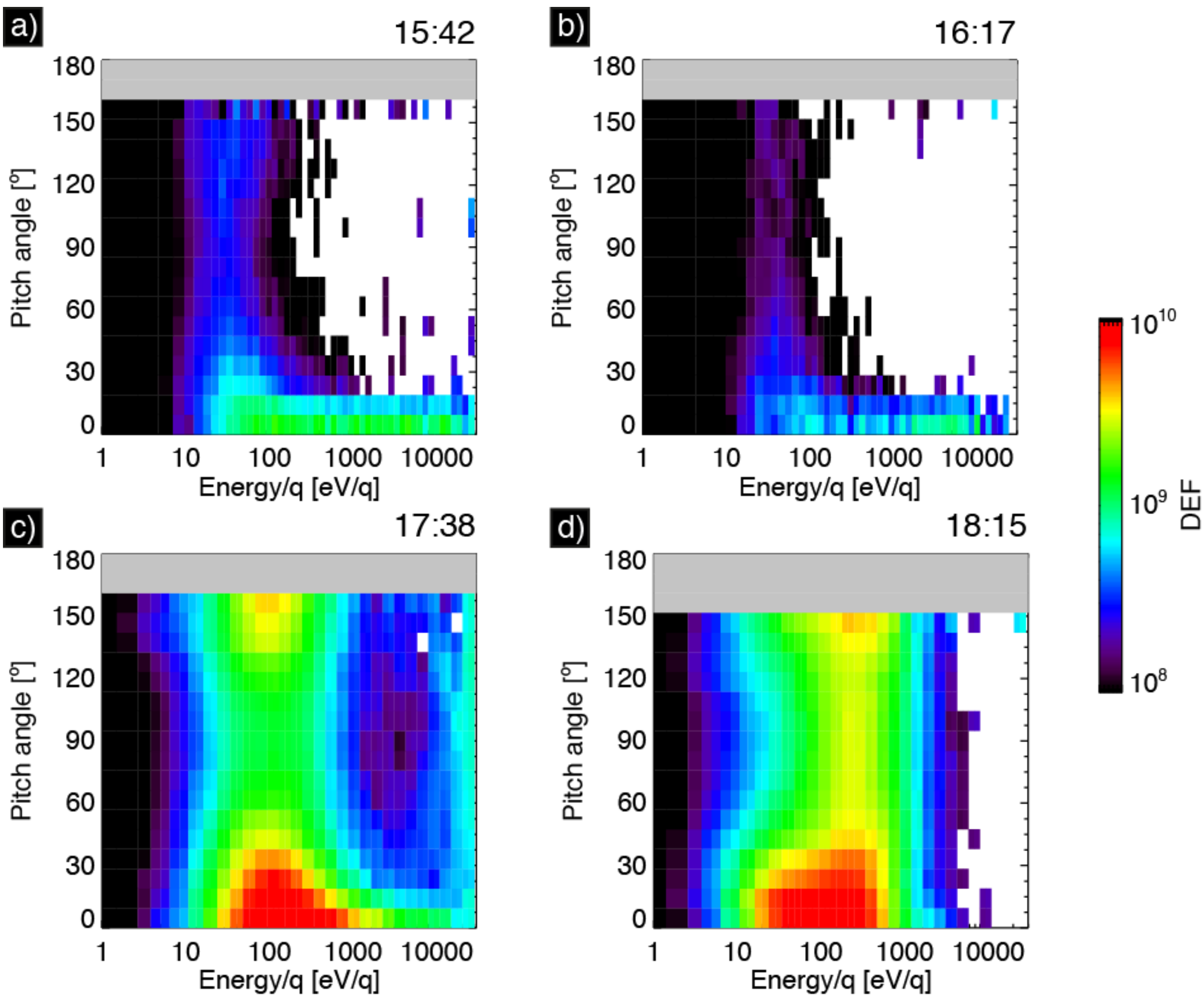

Figure S13: Electron pitch angle distributions near the lobe showing electrons forming a beam flowing parallel to the magnetic field (0º pitch angle) near the lobe/plasma sheet

© 2015 Macmillan Publishers Limited. All rights reserved

boundary (a and c), in the lobe (b), and returning to a bidirectional ~100 eV population in the plasma sheet.

© 2015 Macmillan Publishers Limited. All rights reserved